



Cite this: *CrystEngComm*, 2016, 18, 1996

## Crystal structure, microstructure and electrochemical properties of hydrothermally synthesised $\text{LiMn}_2\text{O}_4$ †

Troels Lindahl Christiansen, Espen D. Bøjesen, Martin Søndergaard, Steinar Birgisson, Jacob Becker and Bo B. Iversen\*

The hydrothermal synthesis method offers an environmentally benign way of synthesizing Li-ion battery materials with strong control of particle size and morphology, and thereby also the electrochemical performance. Here we present an in depth investigation of the crystal structure, microstructure and electrochemical properties of hydrothermally synthesized  $\text{LiMn}_2\text{O}_4$ , which is a widely used cathode material. A range of samples were synthesized by a simple, single-step hydrothermal route, and the products were characterized by elaborate Rietveld refinement of powder X-ray diffraction data, electron microscopy and electrochemical analysis. A distinct bimodal crystallite size distribution of  $\text{LiMn}_2\text{O}_4$  was formed together with a  $\text{Mn}_2\text{O}_3$  impurity. At high LiOH concentration the layered  $\text{Li}_x\text{Mn}_y\text{O}_2$  phase was formed. The crystallite sizes and impurity weight fractions were found to be highly synthesis dependent, and the amount of spinel impurity phase was found to correlate with deterioration of the electrochemical performance. The  $\text{Mn}_2\text{O}_3$  phase can be very difficult to quantify in standard powder X-ray diffraction and due to peak overlap and X-ray fluorescence impurity levels of more than 10% are easily hidden. Furthermore, the spinel  $\text{LiMn}_2\text{O}_4$  phase can easily be mistaken for the layered  $\text{Li}_x\text{Mn}_y\text{O}_2$  phase. The present study therefore highlights the importance of thorough structural characterization in studies of battery materials.

Received 2nd December 2015,  
Accepted 17th February 2016

DOI: 10.1039/c5ce02358k

[www.rsc.org/crystengcomm](http://www.rsc.org/crystengcomm)

## Introduction

Li-ion battery technology has developed into an integral part of modern society, fulfilling the needs for portable energy storage in devices such as tablets, cell phones, laptops and potentially also in larger scale mobile energy storage applications including electric vehicles and possibly large scale grid storage of renewable energy.<sup>1</sup> An indispensable step on the way towards exploitation of the full potential of the Li-ion battery technology is the development of high-performance electrodes. Many of the cathodes used in Li-ion batteries are based on intercalation compounds. Among these intercalation cathodes three structures stand out as the most prevalent i) olivine structures ( $\text{LiFePO}_4$ ), ii) layered  $\text{LiCoO}_2$  structures and iii) spinel type structures ( $\text{LiMn}_2\text{O}_4$ ).<sup>2</sup> A common feature of these intercalation cathodes is that  $\text{Li}^+$ -ions can diffuse

easily in and out of the host framework structure without causing a significant destabilization of the framework.

Commercially, the layered  $\text{LiCoO}_2$  compound has been widely used; however it poses some serious safety and environmental hazards, combined with a relatively high cost. The cheaper, safer and more environmentally benign alternative spinel type  $\text{LiMn}_2\text{O}_4$  (LMO) cathode has been commercialized in an effort to alleviate these issues.<sup>3–5</sup> A plethora of  $\text{LiMn}_2\text{O}_4$  synthesis methods have been reported in literature.<sup>6–13</sup> It has, in many cases, been shown that a strong correlation between the nano- and microstructure of the product and the electrochemical performance exists.<sup>14–17</sup> Thus, when choosing a synthesis method it should be considered how the given method affects particle size and morphology.<sup>18–20</sup> Studies have proven hydrothermal synthesis effective in achieving some degree of control of particle size and morphology for a vast amount of different advanced functional materials, including materials relevant to  $\text{Li}^+$  ion battery technology.<sup>21–26</sup> One important aspect of the hydrothermal process is the possibility of tuning structural and microstructural features of the synthesized products by varying different reaction parameters including precursor concentration, pH, temperature, synthesis time, and reaction pressure. Furthermore, the comparatively low energy requirements and fast reaction rates achievable

Department of Chemistry and iNANO, Aarhus University, DK-8000 Aarhus C, Denmark. E-mail: [bo@chem.au.dk](mailto:bo@chem.au.dk)

† Electronic supplementary information (ESI) available: Voltage vs. capacity curves for LMO-3.5h and LMO-24h, additional TEM pictures, PXRD patterns showing effects of LiOH precursor concentration and Rietveld refinements and refined parameters for all LMO samples. See DOI: 10.1039/c5ce02358k

renders the hydrothermal method commercially as well as scientifically interesting.<sup>27–31</sup>

In this study we investigate the hydrothermal synthesis and characterization of LMO. Several obstacles regarding the characterization of these types of materials were encountered and our paper has focus on identifying and alleviating these.<sup>32–35</sup> One particular concern is accurate phase analysis with powder X-ray diffraction (PXRD) in the presence of strong fluorescence (high background). It is shown that seemingly minor impurity contents can be deceptive, and that proper Rietveld modelling and multi-method analysis are necessary to obtain a correct material characterization.<sup>27</sup>

Hydrothermal synthesis of LMO was first presented by Liddle *et al.*,<sup>36</sup> and three structures are relevant when discussing the synthesis products: spinel  $\text{LiMn}_2\text{O}_4$ , layered  $\text{Li}_x\text{Mn}_y\text{O}_2$  and spinel  $\text{Mn}_3\text{O}_4$ , the latter often referred to by the mineral name, hausmannite. Spinel  $\text{LiMn}_2\text{O}_4$  (Fig. 1) features cubic close-packed oxygen ions occupying the 32e positions and Li ions occupying one-eighth of the tetrahedral 8a sites while Mn occupies half of the octahedral 16d sites.<sup>37,38</sup> The framework can thus be viewed as  $[\text{MnO}_6]$  octahedra sharing edges, and in this fashion forming channels allowing  $\text{Li}^+$  ion diffusion.<sup>39</sup> The manganese cations in the structure are assumed to be equally divided between the oxidation states +3 and +4 and randomly distributed on the 16d sites, resulting in an average manganese oxidation state of +3.5. Approximately at room temperature, and dependent on the thermal history of a given sample,  $\text{LiMn}_2\text{O}_4$  can undergo a phase transition upon cooling to a rhombohedral structure ( $Fdd\bar{d}$ ) and at even lower temperatures to the tetragonal structure ( $I4_1/amd$ ). These transitions occur due to charge ordering of the Mn ions and the accompanying effect of the Jahn–Teller distortion of the  $\text{Mn(III)}$  ions.<sup>40,41</sup> Cycling of  $\text{LiMn}_2\text{O}_4$  in a battery cell entails changing between the two oxidation states, but the cycling mechanism is quite complicated. The complexity arises primarily due to the Jahn–Teller active  $\text{Mn(III)}$  ions. Increasing amounts of  $\text{Mn(III)}$  in the structure will cause an increase of the  $c/a$  ratio of up to 16% and consequently cause a cubic to tetragonal phase transition. Moreover, the  $\text{Mn(III)}$  ions undergo disproportionation at the surface of the LMO particles. Both factors contribute to a limitation of the practical voltage range in battery cells based on this compound.<sup>42</sup>

Layered  $\text{Li}_x\text{Mn}_y\text{O}_2$  crystallizes in the  $R\bar{3}m$  space group and is iso-structural with  $\text{LiCoO}_2$ , however containing Li and Mn

vacancies due to stoichiometric deviations. Similarly to  $\text{LiMn}_2\text{O}_4$ ,  $\text{Li}_x\text{Mn}_y\text{O}_2$  can be envisaged to consist of edge sharing  $[\text{MnO}_6]$ -octahedra. However, these only share edges within single layers and thus no three dimensional  $[\text{MnO}_6]$  based framework exists. The layers are stacked alternately with Li ions along the  $c$  direction.  $\text{Li}_x\text{Mn}_y\text{O}_2$  offers a higher gravimetric capacity compared with the spinel phase, owing to the more favourable Li/Mn ratio of the layered structure.<sup>43</sup> During cycling, the layered structure readily converts to the more stable spinel-type by diffusion of Mn-ions into the Li-ion containing layers. This structural transition occurs with ease due to the similarities of the two structures and is not reversible. Both structures contain the same cubic-close packed oxygen sub lattice, and thus the conversion only entails diffusion of the mobile cations.<sup>5,43,44</sup> The layered structure is of limited commercial interest and remains mainly of interest as a precursor stage for the spinel  $\text{LiMn}_2\text{O}_4$  phase.

The close relation between the two structure types, and thus their very similar PXRD patterns, has previously been highlighted for the  $\text{LiCoO}_2$  based analogues. For these cobalt compounds a low-temperature variant with 6% of the Co atoms located in the Li layers, was modeled equally well by Rietveld refinements based on either the  $R\bar{3}m$  space group or  $Fd\bar{3}m$  space group.<sup>45</sup> The PXRD patterns of the Mn-based structures also exhibit many resemblances to each other.

$\text{Mn}_3\text{O}_4$  can crystallize in a spinel type structure, and like the aforementioned structures, it features a  $ccp$  lattice of oxygen. In  $\text{Mn}_3\text{O}_4$ ,  $\text{Mn(II)}$  resides in the tetrahedral sites while  $\text{Mn(III)}$  is located at the octahedral positions.<sup>46</sup> This particular manganese oxide is a common impurity formed when synthesizing Li–Mn–O compounds by wet chemical methods *e.g.* due to non-stoichiometry, lacking Li incorporation or redox related issues. In a recent *in situ* PXRD study we have used a similar synthesis method as in the present work to show the prevalence of  $\text{Mn}_3\text{O}_4$  formation during synthesis.<sup>28</sup>

## Experimental

### Synthesis

All samples were prepared in steel autoclaves lined with a 19 mL Teflon insert using a synthesis method similar to the one presented by Liddle *et al.*<sup>36</sup> 0.2157 g  $\text{KMnO}_4$  (*p.a.* Merck) was dissolved in 10.5 mL 0.10 M  $\text{LiOH}$  ( $\text{LiOH}\cdot\text{H}_2\text{O}$  (*p.a.* Bie&Berntsen A/S)). 0.125 mL ethanol (96%) was added as reducing agent. The ~60% filled autoclave was placed in a preheated furnace at 180 °C for times ranging from 2 h to 48 h. After the respective reaction time had elapsed the autoclaves were removed from the furnace and allowed to cool to room temperature by convection. The product was washed and centrifuged with demineralized water three times to remove any water-soluble impurities. The samples are named based on their synthesis time *i.e.* LMO-3.5h, LMO-4.3h, *etc.*

For evaluation of electrochemical performance, galvanostatic cycling was performed on CR2032 type half-cells. The half-cells were assembled with Li-metal foil as counter and reference electrode, and two pieces of 25  $\mu\text{m}$

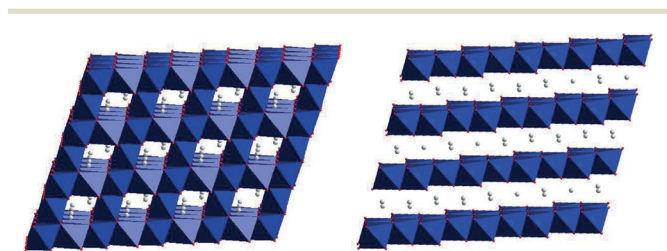


Fig. 1 The crystal structures of (left) spinel  $\text{LiMn}_2\text{O}_4$  and (right)  $\text{Li}_x\text{Mn}_y\text{O}_2$  depicted with blue  $[\text{MnO}_6]$ -octahedra.

porous polypropylene membranes as separator. The electrolyte was 1 mol L<sup>-1</sup> LiPF<sub>6</sub> in ethylene carbonate (EC) and dimethyl carbonate (DMC) in the ratio of 1:1 by volume. For the working electrode, the active material was mixed with SuperP conducting carbon and polyvinylidene difluoride (PVDF) in the weight ratio of 76:12:12 and coated onto aluminium-foils giving a thickness of the dry layer of ~30 μm. The working electrodes were compressed with ~40 kN cm<sup>-2</sup>. The cells were assembled in a glove box with water and oxygen levels at ~1 ppm. After assembly the cells were charged and discharged at various currents between 3.5 V and 4.3 V.

### Synchrotron PXRD

High-resolution synchrotron PXRD data were collected on the large Debye–Scherrer image plate diffractometer at beamline BL44B2, SPring8, Japan, using  $\lambda = 0.499818(4)$  Å. The powders were filled in 0.3 mm glass capillaries and spun during measurements. The higher signal to noise ratio and  $q$ -space resolution of the synchrotron data compared with the in-house parallel-beam setup comes at the cost of a more uneven background due to the use of glass capillaries as sample containers.

### In-house PXRD

In-house PXRD data were collected using a Rigaku Smartlab diffractometer fitted with a rotating Cu anode. Parallel beam optics with a Ge(220) double-bounce monochromator, 5 mm incident slit, soler 5° incident optic and soler 5°/1D receiving optic were employed to achieve the best possible trade-off between resolution and intensity. A D/tex Ultra PSD detector with fluorescence suppression was used.

For comparison, data were also collected on the same Rigaku Smartlab diffractometer, but in a standard configuration that measures data similar to many data in the literature. This includes parallel beam geometry without monochromatization of the incident beam. Furthermore, no fluorescence suppression was used on the detector and the incident slit size was set to 10 mm.

### Rietveld refinements

Rietveld refinements were performed using the Fullprof Software suite.<sup>47</sup> The peak profiles were modeled based on a Thompson Cox Hastings pseudo Voigt formalism,<sup>48</sup> incorporating axial divergence asymmetry. The instrumental contribution to the peak profiles were determined by refinement of a NIST LaB<sub>6</sub> standard. All crystallites were modelled as spherical crystallites. Based on TEM images this is a good approximation for one group of crystallites (the smallest), whereas larger platelet-like morphologies were also detected. Due to the complexity of the model, it was decided not to include anisotropic size broadening. Instead the crystallite sizes were determined based on integral breadth methods and the Scherrer equation.<sup>49</sup> The background was modelled by linear interpolation between a set of points with refineable height.

Occupancies, atomic displacement parameters and position were not refined and kept at the values found in literature (LiMn<sub>2</sub>O<sub>4</sub>; ICSD card no. 50415, Mn<sub>3</sub>O<sub>4</sub>; ICSD card no. 002024, Li<sub>0.78</sub>Mn<sub>0.85</sub>O<sub>2</sub> ICSD card no. 173134.). This choice of refined parameters was made to minimize parameter correlation and due to the fact that test refinements including refinement of these parameters led to either unphysical values, non-significant improvements of the fit and convergence issues. Further discussion of the refined models are presented below.

### Transmission electron microscopy

Bright field transmission electron microscopy (TEM) images were recorded using a Philips CM20 electron microscope equipped with a LaB<sub>6</sub> filament at an acceleration voltage of 200 kV and a CCD camera. HR-TEM images were recorded on a TALOS F200A with a TWIN lens system, X-FEG electron source and a Ceta 16M Camera. Diluted samples were prepared by sonication in ethanol and individual drops were placed on the respective TEM grids (200 mesh copper grid with formvar/carbon support film) and dried at ambient conditions.

## Results and discussion

### Data considerations

Interpretation of PXRD data collected on hydrothermally synthesized LMO products, which are often assumed to be pristine LMO, can be challenging. Weakly-scattering Li, X-ray fluorescence from Mn and synthesis impurities with similar structures and complex microstructural features all contribute to this. High-quality data are therefore essential to extraction of reliable structural and microstructural information. Fig. 2 shows a comparison of PXRD data collected using different instruments resulting in data sets of varying quality. There are significant differences in signal to noise ratio, instrumental peak profile resolution and  $q$ -space resolution.

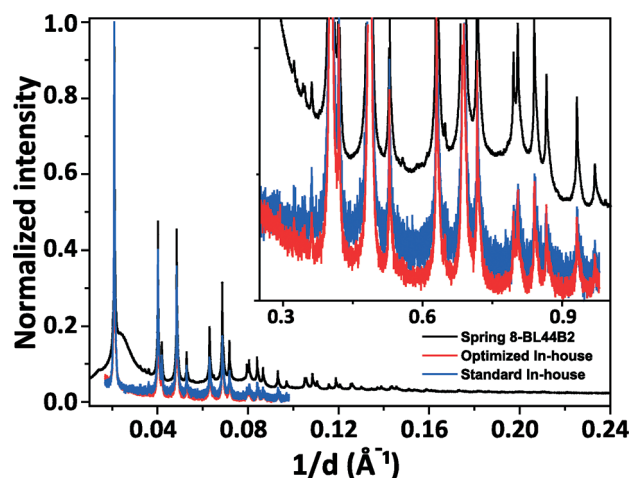


Fig. 2 PXRD patterns collected with different setups, illustrating the differences in data quality achievable. The sample is in all three cases LMO-5h.

Minor impurity peaks clearly visible in the “Spring 8-BL44B2” dataset are nearly indistinguishable from the background in the “standard-in-house” dataset. In the “optimized-in-house” dataset the impurity peaks are barely visible.

### Rietveld modelling of LMO

A complex phase composition was found to be present in all synthesized LMO samples. Three crystalline phases were necessary to achieve a satisfactory Rietveld model: one spinel  $\text{Mn}_3\text{O}_4$  and two LMO phases to describe a bimodal crystallite size distribution which was found to be present in all samples. Within each size distribution, small LMO crystallites (10–30 nm) were found to have ~6–8 % smaller unit cell parameters than the large LMO crystallites (60–120 nm). This combination of two groups of crystallites gives rise to peak profiles being almost super-Lorentzian. Owing to the differences in lattice parameters, the small crystallites contribute with broad tails at high angle in the peak profiles and the large crystallites cause sharper profiles at low angle. The effect on the pattern is illustrated in the insert of Fig. 3.

Refinement of occupancies, positions and other structural parameters provided no reliable explanation for the difference in unit cell parameter between large and small crystallites. Except for the scale factor, no refinement of intensity related parameters were performed due to the appreciable number of parameters and complex phase composition, including large peak overlaps and low scattering contrast between constituents in the samples. One probable origin of the differences in unit cell could be a varying quantity of oxygen vacancies. This relation has been shown previously by neutron scattering experiments.<sup>50</sup> A larger concentration of oxygen vacancies in the structure will decrease the average oxidation state of Mn, which increases the ionic radius and expands the unit cell.

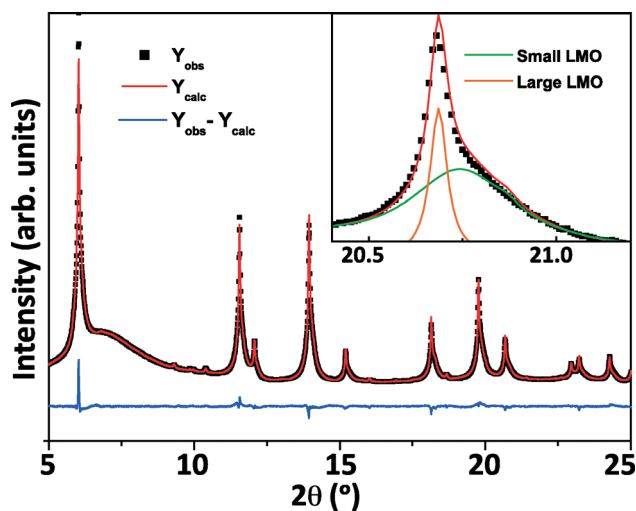


Fig. 3 Rietveld refinement of the Spring8-BL44B2 data of sample LMO-5h, the insert shows the contribution of both LMO phases to the bimodal crystallite size distribution.

SEM studies have previously shown bimodal *particle* size distributions to be a common feature in LMO samples synthesized by hydrothermal methods.<sup>36,50,51</sup> Here we show by PXRD that a bimodal *crystallite* size distribution also exist for LMO from hydrothermal synthesis. PXRD data collection with poor instrumental resolution and low signal to noise ratio will hide this subtle but important feature. The size distribution found using PXRD and Rietveld refinement is supported by TEM images (Fig. 10).

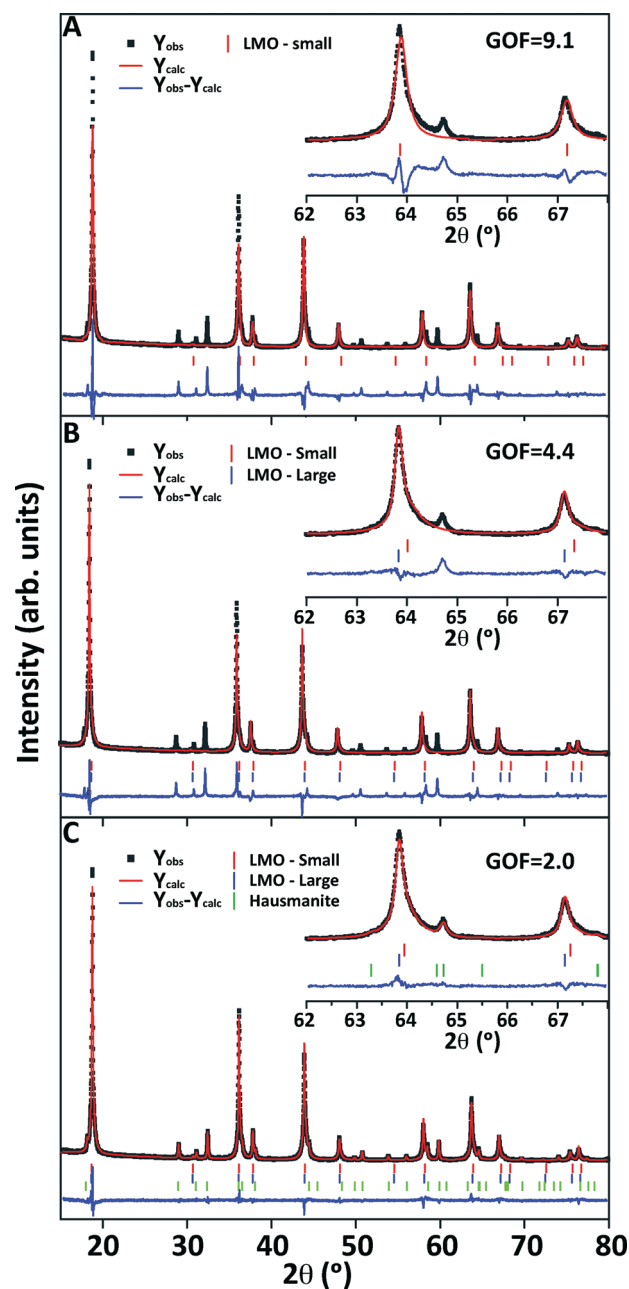


Fig. 4 Rietveld refinement of optimized in house data on LMO-24h containing ~40% hausmannite. Fits using three different models are shown. A) single  $Fd\bar{3}m$  phase B) two  $Fd\bar{3}m$  phases with different sizes C) two  $Fd\bar{3}m$  and the hausmannite phases.



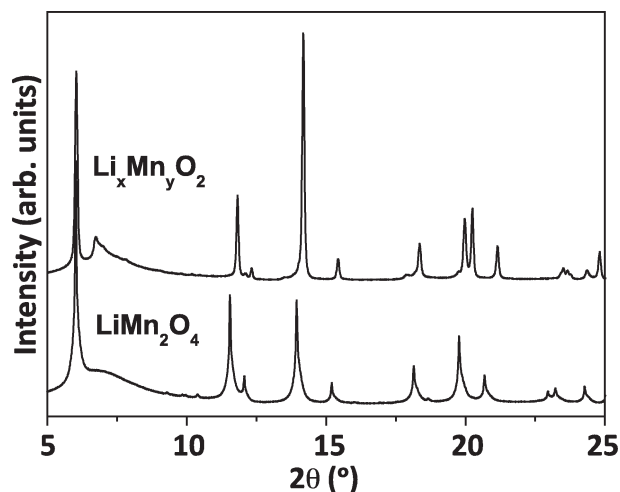


Fig. 5 Synchrotron PXRD patterns of samples (top) LMO-5h-15 and (bottom) LMO-5h. The higher LiOH content in the precursor in LMO-5h-15 results in crystallization in the layered  $R\bar{3}m$  space group instead of the spinel  $Fd\bar{3}m$  space group.

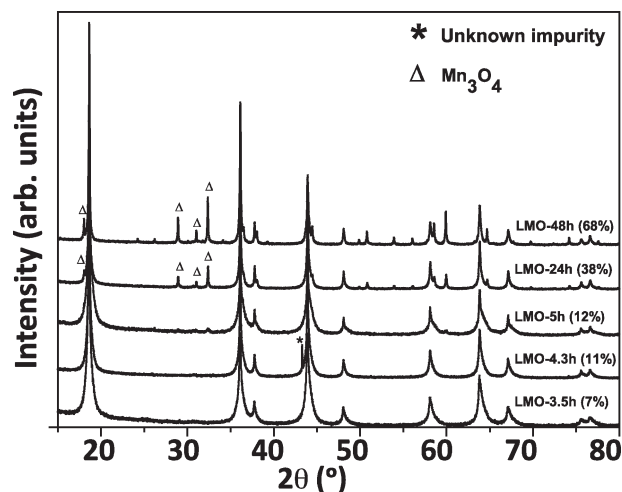


Fig. 7 PXRD patterns of all samples synthesized with varying reaction time. The  $Mn_3O_4$  content extracted via Rietveld refinement is given in parentheses. The data were collected using the optimized in-house setup.

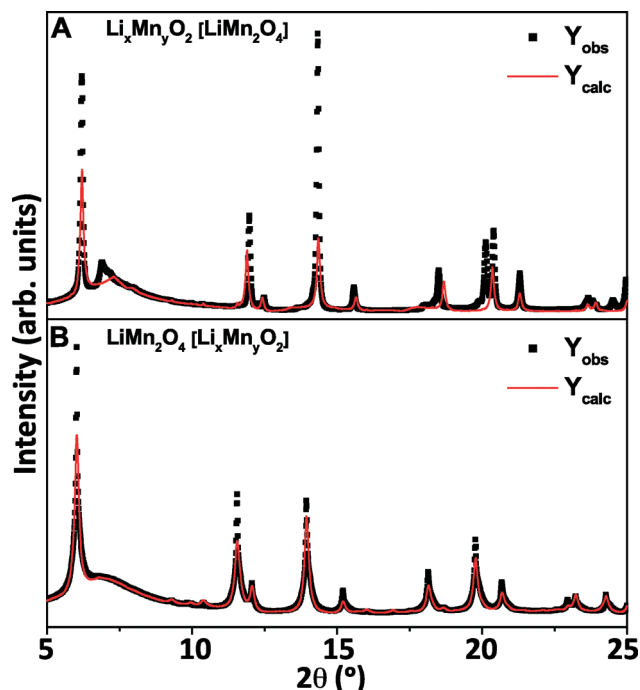


Fig. 6 A) LMO-5h-15 refined with the  $LiMn_2O_4$  model. B) LMO-5h refined with the  $Li_xMn_yO_2$  model.

The effect on the goodness of the fit by inclusion of multiple phases is shown in Fig. 4. In Fig. 4A, a fit based on a single LMO phase is shown. The profile of the peak is not well reproduced by this simple model; asymmetry towards the high angular region is not well described and at least one peak is not accounted for at all. In Fig. 4B a model containing two LMO phases with different crystallite sizes and different unit cell parameters has been applied. Inclusion of the second phase allows for a satisfactory fit of the

asymmetry, but the two-phase model lacks modelling of several peaks *e.g.* at  $\sim 64.6$  degrees. Inclusion of nanocrystalline  $Mn_3O_4$  as a third phase results in a further improved fit, Fig. 4C. The goodness of fit significantly improves upon addition of each phase; going from 9.1 for the single-phase model, 4.4 for the two-phase model and finally 2.0 for the three-phase model. Visual inspection of the fit corroborates the model. However, due to the complex microstructural features, overlapping reflections and limited data quality, the fit is still not perfect. Various issues such as anisotropic morphologies, defects, non-stoichiometry and the fact that measurements were performed at room temperature near the phase transition from cubic to orthorhombic, causes problems; these cannot be solved for the current samples using the present data. Attempts were made at improving the Rietveld model by including more advanced features such as

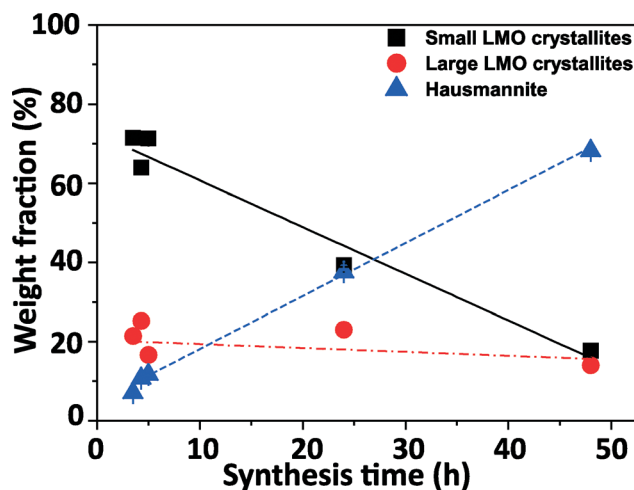


Fig. 8 Weight fraction from refinements as a function of synthesis time, lines are solely ment to act as guides to the eye.

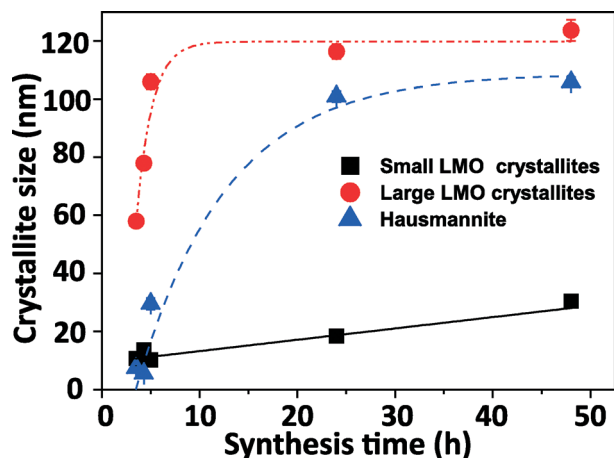


Fig. 9 Crystallite size from refinement as a function of synthesis time.

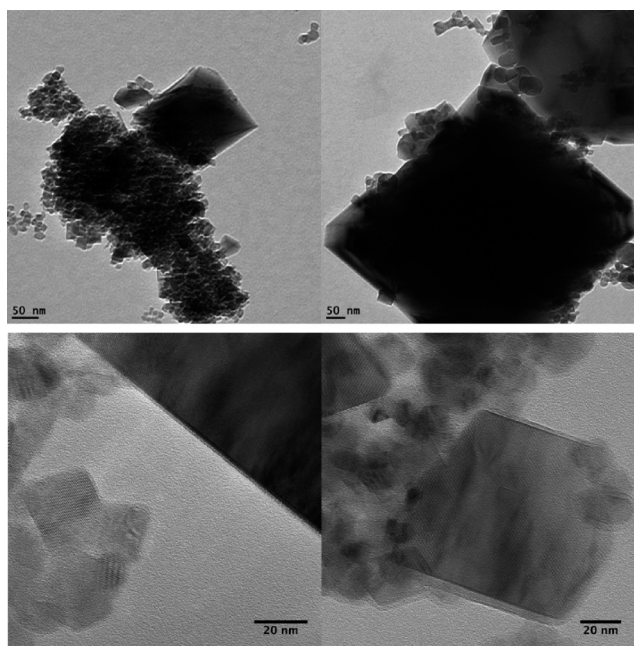


Fig. 10 (Top left) LMO-4.3h, (Top right) LMO-48h, two bottom micrographs show HR-TEM images of the LMO-24h sample, the contrast differences at the edges may be an indication of high defect concentrations or partial production at the surface of the particles.

lowering of the symmetry of the LMO phases, refinements of occupancies and anisotropic crystallite morphology. None of these refinements improved the fits significantly, and these models also possess higher degrees of parametric correlation. Thus, the relatively complex model was kept as simple as possible. The importance of performing Rietveld refinement instead of simple peak search-and-match procedures cannot be emphasized strongly enough. If simple matching of peak positions was used, the bimodal size distribution would not have been detected and a 40%  $\text{Mn}_3\text{O}_4$  impurity would have been unnoticed.

Issues regarding data quality and structural similarities were also observed. These can be exemplified by varying the

Li/Mn ratio in the synthesis procedure. It was found that increasing LiOH concentration 2.5 times or more in the precursor relative to the concentration of  $\text{KMnO}_4$  lead to a gradual change in the composition of the product from mainly LMO towards the layered  $\text{Li}_x\text{Mn}_y\text{O}_2$ . The only phase present at LiOH/ $\text{KMnO}_4$  molar ratios above 7.5 in the precursor was  $\text{Li}_x\text{Mn}_y\text{O}_2$  (see ESI†, Fig. S4). The structural similarity of the two lithium–manganese–oxide phases ( $\text{Li}_x\text{Mn}_y\text{O}_2$  and LMO) is so overwhelming that their PXRD patterns are difficult to distinguish. In this respect, matching of peak positions will often not suffice to distinguish one from the other or to detect mixtures. A demonstration is seen in Fig. 5 which shows synchrotron PXRD patterns for LMO-5h and a  $\text{Li}_x\text{Mn}_y\text{O}_2$  sample synthesized using the same conditions but with 15 times the LiOH concentration (named LMO-5h-15).

In comparison with conventional data collected with a  $\text{CuK}\alpha$  source the displayed  $2\theta$  range is equivalent to approximately  $15\text{--}80^\circ$ . By using the shorter wavelength ( $\sim 0.5 \text{ \AA}$ ) a larger  $q$ -range can be covered, thus allowing for more accurate structural refinements. When inspecting the range covered in a standard laboratory based experiment (Fig. 2) it becomes evident that the diffraction patterns of the two structures are nearly identical within this range. Significant deviations are mainly found as differences in the relative peak intensities, but there is one extra peak in the  $\text{Li}_x\text{Mn}_y\text{O}_2$  pattern at  $2\theta \sim 21^\circ$  that cannot be found in the LMO pattern. There is also an asymmetric peak at  $2\theta \sim 6^\circ$  which is presumably caused by diffuse scattering originating from stacking faults along the  $c$ -axis of the ordered cationic planes.<sup>52</sup>

An effective way of circumventing these types of issues with phase identification is by the use of Rietveld refinement. If an incorrect structural model is applied to PXRD data of a sample, the refinement will only converge slowly, and the quality of the fit can be quantified based on reliability factors. This is demonstrated in Fig. 6 where the layered  $R\bar{3}m$  structural model is applied to data from a LMO sample (LMO-5h) and the spinel  $Fd\bar{3}m$  structural model to a  $\text{Li}_x\text{Mn}_y\text{O}_2$  sample (LMO-5h-15).

For the LMO model applied to the LMO-5h-15 data, the fit is poor, especially the intensities are far off and one peak at  $2\theta \sim 21^\circ$  is left unaccounted for. Moreover, the position of some of the peaks in the model and data coincide, while others do not. This can only be resolved by lowering the symmetry of the model. In contrast the  $\text{Li}_x\text{Mn}_y\text{O}_2$  model applied to LMO-5h is slightly more successful at describing the data, but nevertheless the intensity distribution in the model does not correspond to the data, and only a severe over-parametrization or unphysical values of various parameters can get the model to fit the data. Since the layered  $\text{Li}_x\text{Mn}_y\text{O}_2$  does not find much use in battery applications there will be no further discussion of this phase. In the ESI† a small parameter study of the influence of LiOH on phase composition is given. Nevertheless, it is important to note that the synthesis product can be changed from a spinel to a layered structure simply by raising the LiOH precursor concentration.

## Reaction time study

The ratio between the three different phases varies greatly in the samples with changing synthesis times ranging from 3.5 h to 48 h. No crystalline product was obtained for reaction times shorter than 3.5 h. The most significant effect of increasing reaction time is the presence of the  $\text{Mn}_3\text{O}_4$  phase and the disappearance of the small LMO crystallites. However, this change in phase composition has a surprisingly small impact on the overall appearance of the PXRD patterns of the samples as seen in Fig. 7.

The two samples with the shortest reaction time show no obvious signs of  $\text{Mn}_3\text{O}_4$ , while in the pattern for LMO-5h the only clear signs are the three very low intensity peaks around  $2\theta = 28\text{--}32^\circ$ . In a “standard in-house” measurement these peaks disappear in the background (see Fig. 2) mainly due to the strong X-ray fluorescence from Mn. A significant overlap between the  $\text{Mn}_3\text{O}_4$  and LMO peaks exists and consequently the content of  $\text{Mn}_3\text{O}_4$  seems qualitatively insignificant. The overlap of the two phases is so pronounced that the diffractogram of LMO-48h with a phase fraction of nearly 70%  $\text{Mn}_3\text{O}_4$  still on a first inspection appears to be dominated by LMO. The main reason for this is that the most intense peak of the  $\text{Mn}_3\text{O}_4$  phase at  $2\theta = 36^\circ$  completely overlaps with an intense peak of the LMO phase.

The variation in crystalline phase composition as extracted from refinements is shown in Fig. 8. Samples with a short reaction time consist primarily of small LMO crystallites, although the bimodal size distribution of LMO crystallites was observed in all samples. The fraction of large crystallites remains virtually constant for all synthesis times, whereas the amount of small crystallites decreases significantly.

The weight fraction of  $\text{Mn}_3\text{O}_4$  seems to change almost inversely proportionally to that of the small crystallites, indicating a connection between the appearance of  $\text{Mn}_3\text{O}_4$ , and disappearance of the small crystallites. The refined crystallite sizes for the all samples are plotted in Fig. 9 as a function of reaction time.

The size of all three crystallite fractions increases with synthesis time, albeit at very different rates. The small LMO crystallite average size increases from about 10 nm to 30 nm rather linearly, whereas the large crystallites rapidly increase their average size from about 50 nm to 110 nm, reaching a plateau around this value, increasing only slightly with prolonged reaction time. As for  $\text{Mn}_3\text{O}_4$ , the initial crystallites are roughly the same size as the small LMO crystallites, but with increased reaction times their size increases significantly by comparison. These trends are supported by TEM (additional micrographs can be found in the ESI† Fig. S3). TEM images of LMO-4.3h and LMO-48h are shown in Fig. 10 together with HR-TEM images of LMO-24h. The LMO-4.3h sample has a large fraction of small sized to large-sized particles compared with the LMO-48h sample. The TEM images also confirm the average growth of the particles with time. Moreover, the HR-TEM images of LMO-24h show slight indications of high defect concentrations or partial reduction at

the surface of the particles. It should be noted that TEM micrographs show area weighted particle sizes, and for poly-disperse samples these do not coincide with the volume averaged crystallite sizes determined by PXRD.

Combining the trend in crystallite size shown in Fig. 9, with the weight fractions plotted in Fig. 8, one may suggest a possible explanation for the observed formation of the  $\text{Mn}_3\text{O}_4$  impurity and changes in crystallite sizes. The weight fraction of the small crystallites decreases while the weight fraction of the large crystallites remains stable. Because of the concurrent increase in  $\text{Mn}_3\text{O}_4$  weight fraction it is assumed that the smallest LMO crystallites convert to  $\text{Mn}_3\text{O}_4$  via a solid–solid transformation. The conversion from LMO to  $\text{Mn}_3\text{O}_4$  requires a decrease of the average oxidation state from 3.5 to 2.667. Additionally, Li-ions have to exit the structure accompanied by a rearrangement of a fraction of Mn ions from octahedral positions to tetrahedral positions. The reduction likely takes place on the surface of the crystallites. Comparatively short diffusion paths for lithium out of the structure and a large number of surface sites and defects all contribute to the destabilization of LMO. Small crystallites generally exhibit a higher concentration of all of these components and thus it can be rationalized why the small crystallites convert more readily to  $\text{Mn}_3\text{O}_4$  than the larger ones.

## Electrochemical performance

The LMO samples discussed in the previous sections were tested as cathode material in battery cells. The presence of an impurity of  $\text{Mn}_3\text{O}_4$  will degrade the electrochemical performance due to the fact that  $\text{Mn}_3\text{O}_4$  is not electrochemically active in the same voltage range as LMO.<sup>19</sup> Indeed, previous studies investigating LMO cathodes containing a  $\text{Mn}_3\text{O}_4$  impurity have shown lower specific capacity.<sup>6,20</sup>

The deteriorating effect of  $\text{Mn}_3\text{O}_4$  on the electrochemical performance can be observed in Fig. 12 for four different samples with varying  $\text{Mn}_3\text{O}_4$  phase content. The cells of these samples were cycled five times at C/10, C/2, C, 5C and 10C followed by 50 cycles at 1C ( $1\text{C} = 148\text{ mA g}^{-1}$ ). The voltage *versus* capacity for the first two cycles for the samples LMO-4.3h and LMO-48h is shown in Fig. 11 (voltage *versus* capacity curves for LMO-3.5h and LMO-24h can be seen in Fig. S1 in the ESI†). The charge–discharge curves for both samples exhibit the two-plateau behaviour characteristic for the LMO cathode that has been described in detail elsewhere.<sup>53</sup> The curves show no sign of  $\text{Mn}_3\text{O}_4$  being electrochemically active within the voltage windows as has been shown before.<sup>54</sup> A significantly higher first cycle discharge capacity of  $99.2\text{ mA h g}^{-1}$  for the LMO-4.3h sample compared with  $43.2\text{ mA h g}^{-1}$  for LMO-48h is shown in Fig. 11. The LMO-4.3h (along with LMO-24h see ESI† Fig. S2) show a huge irreversible charge capacity at low potential on the first delithiation, which probably is due to a short circuit of the cell during assembly as the PXRD did not show any sign of  $\text{Li}_{2-x}\text{Mn}_2\text{O}_4$ . The short circuit resulted in an overlithiation of the LMO

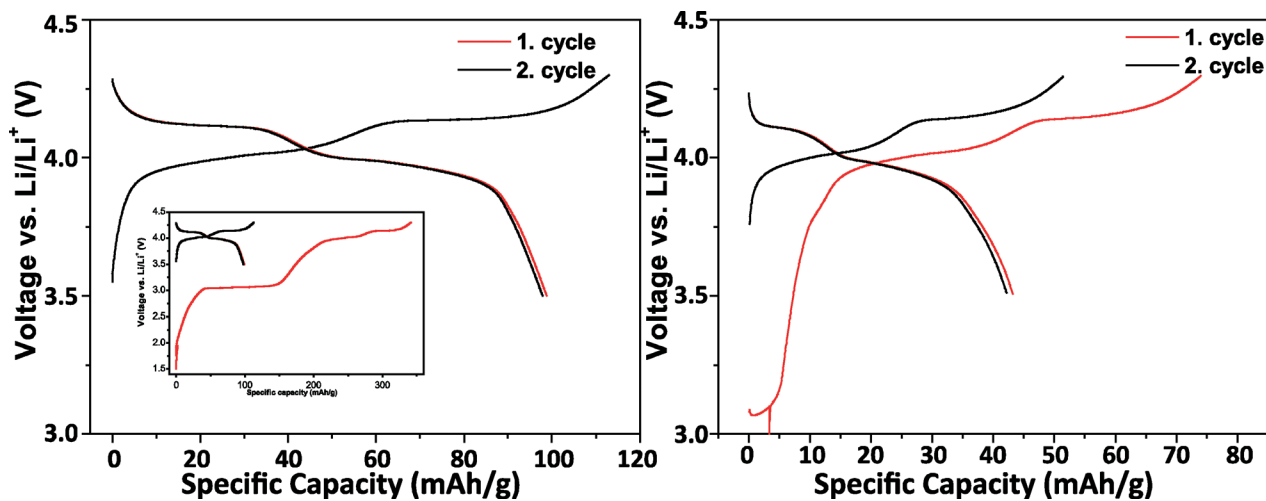


Fig. 11 Voltage versus capacity curves for the first two cycles of LMO-4.3h (left) and LMO-48h (right) discharged between 3.5 V and 4.3 V at C/10.

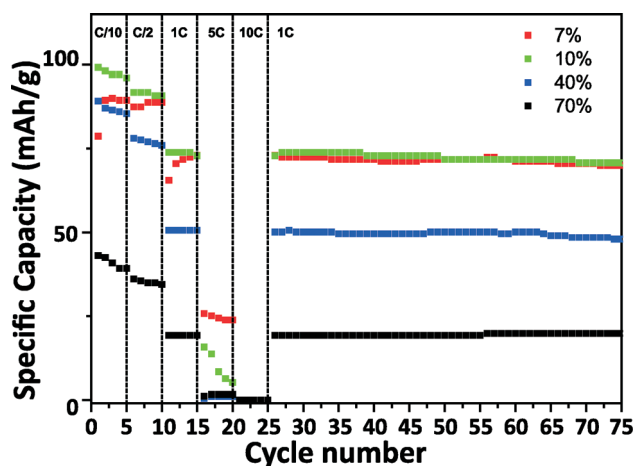


Fig. 12 Specific discharge capacity for cathodes from 4 samples with different  $\text{Mn}_3\text{O}_4$  content. Charge and discharge capacity is represented by empty and full squares, respectively. A break point is inserted in the ordinate to include large initial charge capacities.

cathode, which was then removed on the first charge, however, it did not appear to affect the later cycles.

The superior electrochemical performance of the sample with low  $\text{Mn}_3\text{O}_4$  content is highlighted in Fig. 12 where the two samples containing the lowest  $\text{Mn}_3\text{O}_4$  wt% outperform the high  $\text{Mn}_3\text{O}_4$  wt% samples in terms of both capacity and rate capability. At all the tested C-rates the samples with low  $\text{Mn}_3\text{O}_4$  wt% showed a higher capacity, except at 10C where none of the samples showed any capacity. The better rate performance of the LMO-3.5h and LMO-4.3h might also be ascribed to the smaller average crystallite size.

## Conclusions

Rietveld refinement was applied to study the complex crystalline phase composition of hydrothermally synthesized lithium–manganese–oxide materials. The samples were shown to

consist of either spinel LMO with a bimodal crystallite size distribution and a  $\text{Mn}_3\text{O}_4$  impurity or layered  $\text{Li}_x\text{Mn}_y\text{O}_2$  at high LiOH concentrations. Upon increased reaction time the weight percentage of  $\text{Mn}_3\text{O}_4$  increased, and this was demonstrated to have a significant impact on the electrochemical performance of cathodes made from the synthesis product. Detection and quantification of the  $\text{Mn}_3\text{O}_4$  impurity is difficult due to the high degree of structural similarity between LMO and  $\text{Mn}_3\text{O}_4$ . The intensity of the few non-overlapping  $\text{Mn}_3\text{O}_4$  peaks are in the order of the background noise in standard in-house PXRD measurement. When examining the literature on hydrothermally synthesized LMO it is evident that the experimental capacities generally are appreciably lower than the theoretical capacity of  $148 \text{ mA h g}^{-1}$ . It is likely that some of this discrepancy can be explained by large impurity fractions of  $\text{Mn}_3\text{O}_4$ , which is undetected and thus not accounted for.

This present study highlights the necessity of doing Rietveld refinements on PXRD data instead of settling for “fingerprint” identification of crystalline phases. This is especially true for samples where structurally closely related impurities exist, and for samples that exhibit X-ray fluorescence.

## Acknowledgements

This work was supported by the Danish National Research Foundation (Center for Materials Crystallography, DNRF93) and the Danish Research Council for Nature and Universe (Danscatt). The synchrotron radiation experiment at the SPring-8 synchrotron was conducted with the approval of the Japan Synchrotron Radiation Research Institute. The RIKEN-SPring8 Center is thanked for access to the BL44B2 beamline, and Anders Blichfeld is thanked for data collection.

## Notes and references

- 1 V. Etacheri, R. Marom, R. Elazari, G. Salitra and D. Aurbach, *Energy Environ. Sci.*, 2011, **4**, 3243.



- 2 T. Ohzuku and R. J. Brodd, *J. Power Sources*, 2007, **174**, 449.
- 3 H. Xia, Z. Luo and J. Xie, *Prog. Nat. Sci.*, 2012, **22**, 572.
- 4 O. K. Park, Y. Cho, S. Lee, H.-C. Yoo and H.-K. Song, *Energy Environ. Sci.*, 2011, **4**, 1621.
- 5 B. L. Ellis, K. T. Lee and L. F. Nazar, *Chem. Mater.*, 2010, **22**, 691.
- 6 X. Zhang, H. Zheng, V. Battaglia and R. L. Axelbaum, *J. Power Sources*, 2011, **196**, 3640.
- 7 P. Ragupathy, H. N. Vasan and N. Munichandraiah, *Mater. Chem. Phys.*, 2010, **124**, 870.
- 8 C.-Z. Lu and G. T.-K. Fey, *J. Phys. Chem. Solids*, 2006, **67**, 756.
- 9 B. J. Hwang, R. Santhanam and D. G. Liu, *J. Power Sources*, 2001, **97–98**, 443.
- 10 C. Wan, Y. Nuli, J. Zhuang and Z. Jiang, *Mater. Lett.*, 2002, **56**, 357.
- 11 X. Zhou, M. Chen, H. Bai, C. Su, L. Feng and J. Guo, *Vacuum*, 2014, **99**, 49.
- 12 M. Qian, J. Huang, S. Han and X. Cai, *Electrochim. Acta*, 2014, **120**, 16.
- 13 K. Chen, A. C. Donahoe, Y. D. Noh, K. Li, S. Komarneni and D. Xue, *Ceram. Int.*, 2014, **40**, 3155.
- 14 X. Lv, S. Chen, C. Chen, L. Liu, F. Liu and G. Qiu, *Solid State Sci.*, 2014, **31**, 16.
- 15 A. S. Arico, P. Bruce, B. Scrosati, J.-M. Tarascon and W. van Schalkwijk, *Nat. Mater.*, 2005, **4**, 366.
- 16 H. Uchiyama, E. Hosono, H. Zhou and H. Imai, *J. Mater. Chem.*, 2009, **19**, 4012.
- 17 M. J. Armstrong, C. O'Dwyer, W. J. Macklin and J. D. Holmes, *Nano Res.*, 2013, **7**, 1.
- 18 R. Pitchai, V. Thavasi, S. G. Mhaisalkar and S. Ramakrishna, *J. Mater. Chem.*, 2011, **21**, 11040.
- 19 M. M. Thackeray, W. I. F. David, P. G. Bruce and J. B. Goodenough, *Mater. Res. Bull.*, 1983, **18**, 461–472.
- 20 C. C. Peng, H. L. Bai, M. W. Xiang, C. W. Su, G. Y. Liu and J. M. Guo, *Int. J. Electrochem. Soc.*, 2014, **9**, 1791–1798.
- 21 Z. Cai, L. Xu, M. Yan, C. Han, L. He, K. M. Hercule, C. Niu, Z. Yuan, W. Xu, L. Qu, K. Zhao and L. Mai, *Nano Lett.*, 2015, **15**, 738.
- 22 H. Sun, M. Ahmad and J. Zhu, *Electrochim. Acta*, 2013, **89**, 199.
- 23 Z. Dai, L. Wang, X. He, F. Ye, C. Huang, J. Li, J. Gao, J. Wang, G. Tian and M. Ouyang, *Electrochim. Acta*, 2013, **112**, 144.
- 24 E. D. Bojesen, K. M. Ø. Jensen, C. Tyrsted, N. Lock, M. Christensen and B. B. Iversen, *Cryst. Growth Des.*, 2014, **14**, 2803.
- 25 H. L. Andersen, K. M. Ø. Jensen, C. Tyrsted, E. D. Bojesen and M. Christensen, *Cryst. Growth Des.*, 2014, **14**, 1307.
- 26 K. Byrappa and T. Adschiri, *Prog. Cryst. Growth Charact. Mater.*, 2007, **53**, 117.
- 27 K. M. O. Jensen, M. Christensen, H. P. Gunnlaugsson, N. Lock, E. D. Bojesen, T. Proffen and B. B. Iversen, *Chem. Mater.*, 2013, **25**, 2282.
- 28 S. Birgisson, K. M. Jensen, T. L. Christiansen, J. F. von Bulow and B. B. Iversen, *Dalton Trans.*, 2014, **43**, 15075.
- 29 M. Sondergaard, E. D. Bojesen, M. Christensen and B. B. Iversen, *Cryst. Growth Des.*, 2011, **11**, 4027.
- 30 T. Adschiri, Y. W. Lee, M. Goto and S. Takami, *Green Chem.*, 2011, **13**, 1380.
- 31 K. M. O. Jensen, C. Tyrsted, M. Bremholm and B. B. Iversen, *ChemSusChem*, 2014, **7**, 1594.
- 32 J. Yao, L. Lv, C. Shen, P. Zhang, K.-F. Aguey-Zinsou and L. Wang, *Ceram. Interfaces*, 2013, **39**, 3359.
- 33 H. M. Wu, J. P. Tu, Y. F. Yuan, X. T. Chen, J. Y. Xiang, X. B. Zhao and G. S. Cao, *J. Power Sources*, 2006, **161**, 1260.
- 34 K. Kanamura, K. Dokko and T. Kaizawa, *J. Electrochem. Soc.*, 2005, **152**, A391.
- 35 Y. Cui, W. Bao, Z. Yuan, Q. Zhuang and Z. Sun, *J. Solid State Electrochem.*, 2012, **16**, 1551.
- 36 B. J. Liddle, S. M. Collins and B. M. Bartlett, *Energy Environ. Sci.*, 2010, **3**, 1339.
- 37 M. M. Thackeray, A. de Kock and W. I. F. David, *Mater. Res. Bull.*, 1993, **28**, 1041.
- 38 M. M. Thackeray, L. A. de Picciotto, A. de Kock, P. J. Johnson, V. A. Nicholas and K. T. Adendorff, *J. Power Sources*, 1987, **21**, 1.
- 39 M. O. Filso, M. J. Turner, G. V. Gibbs, S. Adams, M. A. Spackman and B. B. Iversen, *Chem. – Eur. J.*, 2013, **19**, 15535.
- 40 J. Rodriguez-Carvajal, G. Rousse, C. Masquelier and M. Hervieu, *Phys. Rev. Lett.*, 1998, **81**, 4660.
- 41 J. Akimoto, Y. Takahashi, N. Kijima and Y. Gotoh, *Solid State Ionics*, 2004, **172**, 491.
- 42 G. G. Amatucci, N. Pereira, T. Zheng and J.-M. Tarascon, *J. Electrochem. Soc.*, 2001, **148**, A171.
- 43 A. R. Armstrong, A. J. Paterson, A. D. Robertson and P. G. Bruce, *Chem. Mater.*, 2002, **14**, 710.
- 44 A. R. Armstrong, A. J. Paterson, N. Dupré, C. P. Grey and P. G. Bruce, *Chem. Mater.*, 2007, **19**, 1016.
- 45 R. Gummow, D. Liles and M. Thackeray, *Mater. Res. Bull.*, 1993, **28**, 235.
- 46 in *Chemistry of the Elements*, ed. N. N. Greenwood and A. Earnshaw, Butterworth-Heinemann, Oxford, 2nd edn, 1997, p. 1040, DOI: 10.1016/B978-0-7506-3365-9.50030-4.
- 47 J. Rodriguez-Carvajal, *Phys. B*, 1993, **192**, 55.
- 48 P. Thompson, D. E. Cox and J. B. Hastings, *J. Appl. Crystallogr.*, 1987, **20**, 79.
- 49 B. E. Warren, *X-ray diffraction*, Dover Publications, New York, Dover edn., 1990.
- 50 X. Hao, O. Gourdon, B. J. Liddle and B. M. Bartlett, *J. Mater. Chem.*, 2012, **22**, 1578.
- 51 J. F. von Bülow, H.-L. Zhang and D. E. Morse, *Adv. Energy Mater.*, 2012, **2**, 277.
- 52 A. Boulineau, L. Croguennec, C. Delmas and F. Weill, *Chem. Mater.*, 2009, **21**, 4216.
- 53 W. Liu, K. Kowal and G. C. Farrington, *J. Electrochem. Soc.*, 1998, **145**, 459.
- 54 H. Wang, L.-F. Cui, Y. Yang, H. Sanchez Casalongue, J. T. Robinson, Y. Liang, Y. Cui and H. Dai, *J. Am. Chem. Soc.*, 2010, **132**, 13978.